



# Dispersal kernel estimation: A comparison of empirical and modelled particle dispersion in a coastal marine system



Janelle M. Hrycik<sup>a,\*</sup>, Joël Chassé<sup>b</sup>, Barry R. Ruddick<sup>a</sup>, Christopher T. Taggart<sup>a</sup>

<sup>a</sup> Department of Oceanography, Dalhousie University, 1355 Oxford Street, P.O. Box 15000, Halifax, Nova Scotia, B3H 4R2 Canada

<sup>b</sup> Fisheries and Oceans Canada, Gulf Fisheries Centre, 343 University Avenue, P.O. Box 5030, Moncton, New Brunswick, E1C 9B6 Canada

## ARTICLE INFO

### Article history:

Received 8 April 2013

Accepted 26 June 2013

Available online 27 July 2013

### Keywords:

dispersal kernel  
Lagrangian particle tracing  
empirical-model comparisons  
advection and diffusion  
marine  
connectivity

## ABSTRACT

Early life-stage dispersal influences recruitment and is of significance in explaining the distribution and connectivity of marine species. Motivations for quantifying dispersal range from biodiversity conservation to the design of marine reserves and the mitigation of species invasions. Here we compare estimates of real particle dispersion in a coastal marine environment with similar estimates provided by hydrodynamic modelling. We do so by using a system of magnetically attractive particles (MAPs) and a magnetic-collector array that provides measures of Lagrangian dispersion based on the time-integration of MAPs dispersing through the array. MAPs released as a point source in a coastal marine location dispersed through the collector array over a 5–7 d period. A virtual release and observed (real-time) environmental conditions were used in a high-resolution three-dimensional hydrodynamic model to estimate the dispersal of virtual particles (VPs). The number of MAPs captured throughout the collector array and the number of VPs that passed through each corresponding model location were enumerated and compared. Although VP dispersal reflected several aspects of the observed MAP dispersal, the comparisons demonstrated model sensitivity to the small-scale (random-walk) particle diffusivity parameter ( $K_p$ ). The one-dimensional dispersal kernel for the MAPs had an  $e$ -folding scale estimate in the range of 5.19–11.44 km, while those from the model simulations were comparable at 1.89–6.52 km, and also demonstrated sensitivity to  $K_p$ . Variations among comparisons are related to the value of  $K_p$  used in modelling and are postulated to be related to MAP losses from the water column and (or) shear dispersion acting on the MAPs; a process that is constrained in the model. Our demonstration indicates a promising new way of 1) quantitatively and empirically estimating the dispersal kernel in aquatic systems, and 2) quantitatively assessing and (or) improving regional hydrodynamic models.

© 2013 Elsevier Ltd. All rights reserved.

## 1. Introduction

Early life-stage dispersal influences recruitment in both terrestrial and aquatic species, is a widespread characteristic that spans taxonomic groups, and is especially exhibited by aquatic vertebrates and invertebrates, terrestrial invertebrates, and aquatic and terrestrial plants. It is a fundamental process that contributes to variation in the distribution and abundance of a species (Begon et al., 2006). Biological dispersal refers to the spread of individuals away from a source location through passive and (or) active means, where the passive component is especially important

within a fluid such as air or water. Dispersal affects population dynamics (e.g., the distribution of individuals and ultimately reproduction and recruitment), population genetics (e.g., gene flow), and thus the spatial scale of population connectivity through the exchange of individuals among geographically separated subpopulations (metapopulation) of a species (Clobert et al., 2001; Kinlan and Gaines, 2003). Dispersal is often defined in terms of the dispersal kernel, the function that describes the probability of a particle or propagule moving from some source location to all other locations (Siegel et al., 2003; Nathan, 2006; Cowen et al., 2007; Gawarkiewicz et al., 2007).

The significance of dispersal in explaining the distribution and abundance of marine species has been recognised for at least a century (Hjort, 1914). Marine species exchange individuals, and subsequently genes, among subpopulations mainly through larval dispersal (Kinlan and Gaines, 2003; Sale et al., 2005); however, the dominant scales of dispersal in the ocean are still “not known”

Abbreviations: MAP, magnetically attractive particle; VP, virtual particle;  $K_p$ , small-scale (random-walk) particle diffusivity parameter [ $\text{m}^2 \text{s}^{-1}$ ].

\* Corresponding author.

E-mail addresses: [janelle.hrycik@dal.ca](mailto:janelle.hrycik@dal.ca), [jhrycik@gmail.com](mailto:jhrycik@gmail.com) (J.M. Hrycik).

(Pineda et al., 2007) and knowledge of how marine populations are connected in space and time is thus limited (Largier, 2003; Siegel et al., 2003; Cowen et al., 2005, 2007; Kinlan et al., 2005). The variance in dispersal attributable to physical forces (e.g., advection and diffusion) and biological processes (e.g., spawning, behaviour, and mortality) must be determined to enhance the comprehension of dispersal and connectivity in marine systems (most authors cited above). Here we adopt the generic definitions provided by Levin (2006) wherein dispersal (dispersion) refers to where particles or propagules go (their spread) while connectivity refers to where they come from via dispersal.

Motivations to quantify dispersal and connectivity now include sustainable management of commercially valuable and (or) endangered species, mitigating the spread of invasive species, conservation of biodiversity through the design of marine reserves, prediction of species response to climate change, and evaluating the impact of contaminants (Cowen et al., 2005; Kinlan et al., 2005; Levin, 2006; Aiken et al., 2007; Becker et al., 2007). For example, one of the main factors driving the design and implementation of Marine Protected Areas (MPAs) should be the degree of connectivity among local populations of the species that need protection. With explicit data on larval dispersal, it should be possible to adjust reserve size, placement, and spacing to achieve specific management objectives (Sale et al., 2005; Cowen et al., 2007; Fogarty and Botsford, 2007; Jones et al., 2007). Further, empirical estimates of dispersal are necessary to guide numerical modelling studies that are often the basis of management and conservation decisions. Robust measurements of dispersal in the marine environment are rare, and when they are obtained, they must be used to test the assumptions and hypotheses resulting from such models to strengthen model capabilities and associated inferences (Thorrold et al., 2002; Siegel et al., 2003; Cowen et al., 2005; Aiken et al., 2007; Pineda et al., 2007; Werner et al., 2007; Rasmussen et al., 2009).

In this paper we provide a direct measure of particle (propagule) dispersion in the Northumberland Strait region of the southern Gulf of St. Lawrence and make a direct comparison to dispersion estimates provided by hydrodynamic modelling of the same region. We do so through the use of an advanced technology system that can address and overcome many of the problems associated with conventional tracing technologies (e.g., drifters, dye, current meters, and numerical models) frequently employed to study dispersion (Ruddick and Taggart, 2006, 2011; see [Supplementary Material #1](#)). The system uses magnetically attractive particles (MAPs) and a moored magnetic-collector array that allows us to quantify the passive component of the dispersal kernel at the scale of dispersing early-stage planktonic organisms (days to weeks, km to 100 km), thereby providing the biological null model of larval dispersal. The weak buoyancy and slow rise rate designed in the MAPs provides important properties that allow them to mimic weakly-buoyant, passive propagules. Further, as the passive component of connectivity is driven by advective and diffusive processes, knowledge of the dispersal kernel allows the degree of passive connectivity in time and space to be readily estimated for a defined region.

Given the ubiquitous use of dispersal and connectivity estimates that are based on numerical models, it is exceptionally important to compare the MAP results with similar results provided by an existing high-resolution hydrodynamic model designed for the study area that computes Lagrangian trajectories. In addition to achieving a direct model comparison, assessment, and possible improvement, we perform sensitivity tests related to the variation of a key but generally not well-quantified parameter; small-scale diffusivity. Environmental conditions during MAP experiments vary in an uncontrollable manner such that there will always be unanswered questions about dispersal in conditions different from

those present for any given experiment. The advantage of comparing MAP results with model results, under the same conditions, is that the model predictions can be extrapolated to determine the effects of different environmental conditions (e.g., wind, tide, etc.) on dispersal estimates. Only when this is achieved can the biological influences (e.g., behaviour, mortality, etc.) on dispersal be confidently incorporated and assessed when using such models.

## 2. Methods

### 2.1. Study site

The particle dispersion study was conducted in August 2009 in the Northumberland Strait ([Fig. 1](#) and [S1](#)). The Strait is nominally 20–30 km wide, 30–40 m deep at mid-channel, and separates eastern New Brunswick and Nova Scotia (NS) from Prince Edward Island (PEI). Residual flow through the Strait is normally west to east with a net flow of the order kilometres per day (Lauzier, 1965). Particles (detailed below) were released inside Murray Harbour, PEI and the particle collector array (also detailed below) was deployed from inside the Harbour and out into the eastern Strait; a region that is dynamic and tidally-active and where currents can reach  $1.5 \text{ m s}^{-1}$ , particularly along the Murray Head peninsula. There were variable winds during the study, including the passage of Hurricane Bill through the region two days post-release. [Figure S2](#) illustrates the cyclonic expression of Hurricane Bill and the evolution of the wind-driven surface-drift velocity that we estimated as 3.016% of wind velocity (Csanady, 1982). Wind speed and direction were recorded hourly at Caribou Point, NS (Environment Canada, National Climate Data and Information Archive<sup>1</sup>), on the south side of the Strait. Detailed variations in the wind field velocity components ( $u$  and  $v$ ) over the deployment period are provided in [Figure S3](#).

### 2.2. Magnetically attractive particles (MAPs) and collector array technology

The MAPs are composed of hollow glass ( $\text{SiO}_2$ ) microspheres that provide buoyancy, magnetite ( $\text{Fe}_3\text{O}_4$ ) that provides magnetic attraction, and a food-safe epoxy resin that acts as the binding agent. The particles are typically designed to be spherical, in the 100–500  $\mu\text{m}$  equivalent spherical diameter (esd) size range, with a specific gravity (SG) of 1.00 for freshwater-applications or 1.02 for marine-applications. This design allows them to mimic passive propagules suspended in the surface mixed-layer. When manufactured with colour additives (dyes or pigments) they can be used in multiple-release tracer studies. In this study, the MAPs had a median esd of 195  $\mu\text{m}$  and a geometric mean esd of 200  $\mu\text{m}$  ([Fig. S4](#)), a nominal SG of 1.02, and an average rise rate of  $1\text{--}4 \text{ mm s}^{-1}$  in water with a SG of 1.02. The MAPs used in this study underwent extensive toxicity assay and assessment and were released only when environmentally sound permitting by governing agencies was obtained. It should be noted that the MAPs slowly degrade to their silica and magnetite components.

The MAPs are one component of a system (Ruddick and Taggart, 2006, 2011) that, when coupled with a moored magnetic-collector array, allows the direct measurement of particle dispersion within the array domain. The magnetic-collectors are passive samplers designed to float near the surface and vane into the current such that any MAP suspended in the surface layer that flows through a collector will be captured. Flume studies demonstrated a >90%

<sup>1</sup> [http://climate.weatheroffice.gc.ca/climateData/bulkdata\\_e.html?timeframe=1&Prov=XX&StationID=8990&Year=2009&Month=8&Day=1&format=csv](http://climate.weatheroffice.gc.ca/climateData/bulkdata_e.html?timeframe=1&Prov=XX&StationID=8990&Year=2009&Month=8&Day=1&format=csv).

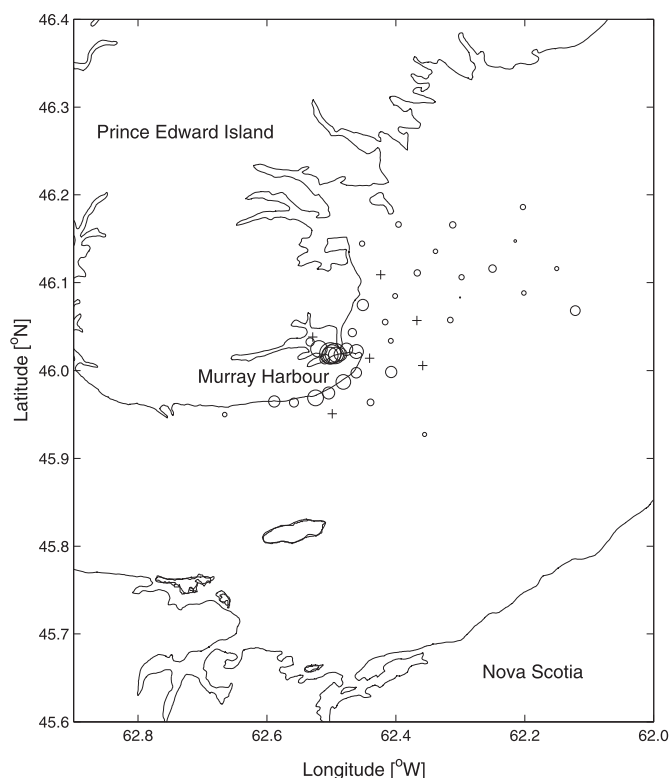


**Fig. 1.** Coastline chart of the eastern Northumberland Strait between Prince Edward Island and Nova Scotia illustrating the location-specific relative number (linearly expanding-area circles with maximum 2450 in Murray Harbour) of MAPs captured among the recovered collectors where the locations of collectors not recovered are denoted by crosses.

probability of MAP capture when passing through a collector at flow speeds less than  $0.8\text{--}1.0\text{ m s}^{-1}$ . The rectangular collector tube is nominally 35 cm long with a square aperture in which the leading end is fitted with strong rare-earth magnets encased within plastic tubes. The collectors used in this study were composed of two superimposed tubes, one near surface and one below surface, each fitted with four magnet tubes with each tube containing two magnets (Fig. S5). The total aperture area was  $86.45\text{ cm}^2$ . The polar-orientation of the magnets within and between the two tubes was designed to maximise the magnetic field for particle capture. Following a point-source release of MAPs and their dispersal over a given period, the magnetic-collectors are recovered and the particles captured by the magnets are enumerated.

The advantage of this system lies in its ability to time-integrate MAPs dispersing through the magnetic-collector array over various time (days to weeks) and space (km to 100 km) scales, and thus the ability to measure long-range dispersion. When large numbers (order  $10^9$ ) are used, the MAPs function as passive particle tracers, where the release point represents a source location and the magnetic-collector array represents the potential dispersal domain. In summary, the system makes use of billions of particle drifters that can be used to estimate dispersion parameters and to make direct comparisons with virtual particle (VP) dispersion estimates provided by hydrodynamic models.

### 2.3. Hydrodynamic modelling

We used a 3D prognostic hydrodynamic modelling system (Saucier and Chassé, 2000; Chassé and Miller, 2010) that incorporates a large-scale 4 km nominal-mesh model covering

the entire Gulf of St. Lawrence region within which is nested a  $200 \times 200\text{ m}$  mesh model that envelops most of the Northumberland Strait (Fig. S1). The low- and high-resolution models employ the same physics, though the time-stepping of the 4 km model is 5 min and that of the 200 m model is 30 s.

The generic code of the model contains a Mellor–Yamada Level II Turbulence closure scheme, a free surface, and semi-implicit solution techniques. There are 32 depth layers (z-levels) in the 4 km model while the 200 m model is limited to 8 z-levels (due to the generally shallow depth of the Northumberland Strait) and has a surface-layer thickness of 2 m. This hydrostatic model is forced by density, tides (five primary constituents input at the boundaries of the 4 km model), observed winds (NCEP, NOAA-CIRES Climate Diagnostics Center, Boulder, CO, USA), observed runoff from the St. Lawrence River measured at Quebec City, and from other rivers, based on monthly climatology interpolated to the model time step, and bulk-formula heat flux. Temperature and salinity are initialised at the beginning of a simulation and are free to evolve with time under forcing. The model calculates horizontal eddy viscosities ( $K_H$ ) using the parameterisation of Smagorinski (1963); i.e., it is dependant on mesh size and on calculated horizontal velocity shear. The calculated values are then used in the momentum and advection-diffusion equations. Thus, the calculated horizontal viscosities are not constant in time or space and a lower bound of  $50\text{ m}^2\text{ s}^{-1}$  is used when applied to the momentum equations to ensure numerical stability of the model.

### 2.4. MAP dispersion

Approximately 30 kg ( $\sim 7.4 \times 10^9$ ) of MAPs were released in the surface layer (0–0.5 m) at a distance of 0.25 km from the nearest shore in the main channel (6 m depth) of Murray Harbour over a 6 h period; 3 h either side of the local flood tide maximum at 10:48 h ADST on 21 August 2009. Subsamples of MAPs suspended in water of regional density were monitored over the study (dispersal) period and the proportion that sunk out of what would have been the surface layer was accounted for in estimating the total number released. Magnetic-collectors had been previously deployed inside the Harbour and over a domain of  $\sim 700\text{ km}^2$  located near the eastern entrance to the Northumberland Strait (Fig. 1). The moored collector array was designed according to deployment and recovery logistics and by using expected winds for the time of year within the hydrodynamic model running in VP tracking mode (see below). A total of 46 collectors were deployed and 40 were recovered after a period of 5–7 d post-release. Upon retrieval, each magnet tube was removed from each collector and stripped of captured MAPs, which were placed in a counting cell and imaged (Fig. S4). The total area ( $\text{mm}^2$ ) of MAPs in each calibrated image was measured using SigmaScan Pro (ver. 5.0). The imaged-area of MAPs captured by each collector was converted to a particle number estimate ( $N_{MAP}$ ) by dividing the imaged-area by the area of a MAP assuming a median diameter of  $195\text{ }\mu\text{m}$  (above).

### 2.5. VP dispersion

Estimating the dispersion of virtual particles in the hydrodynamic model consisted of a point-source release of  $1.92 \times 10^5$  VPs uniformly distributed throughout the 2 m surface layer in the same location in Murray Harbour, on the same date, and over the same 6-hour release period as the MAP release. Corresponding model simulation results at 5, 6 and 7-d periods post-release were used to match the same post-release periods associated with magnetic-collector retrievals. Neither “beaching” nor vertical rise nor sink of VPs was permitted in the model. A small-scale diffusion ( $K_p$ ), achieved by a random walk of VPs, was used to mimic the

horizontal stirring processes that occur on scales smaller than the 200 m grid-scale model is able to resolve. We used constant  $K_p$  values of 0, 2, 5, and 25  $\text{m}^2 \text{s}^{-1}$  among several simulations, as well as minimum values of 50 and 80  $\text{m}^2 \text{s}^{-1}$  based on the Smagorinski (1963) formulations that provide high eddy viscosity values only in areas of very high horizontal shear. Thus,  $K_p$  rarely rises above the minimum  $K_H$  of 50  $\text{m}^2 \text{s}^{-1}$  used in solving the momentum equations.

The model was used to estimate the total number ( $N$ ) of VPs drifting through each grid-cell by calculating an exposition number for each grid-cell over the post-release study period (5, 6, or 7 d). The exposition number ( $E$ ) of a cell ( $ij$ ) is the sum over the individual ( $k$ ) VPs passing through a cell of the distance each VP moved ( $\Delta m$ ) when passing through a cell normalised by the cell length ( $m$ ) according to

$$E_{ij} = \sum_{k=1}^{N_{ij}} \left( \frac{\Delta m_k}{m} \right). \quad (1)$$

## 2.6. MAP and VP comparison

Considering the collectors and model grid-cells as “nets” that capture passing particles, the observed number ( $N$ ) of MAPs or VPs at a location ( $x$ ) of a given magnetic-collector and its corresponding grid-cell can each be considered generically as

$$N = A \int_{t_0}^{t_0+T} C(x, t) \cdot u(x, t) \cdot dt, \quad (2)$$

where  $A$  is the aperture area of a collector or grid cell at  $x$ ,  $C$  is the concentration of MAPs or VPs at  $x$ ,  $u$  is the horizontal flow velocity through a collector or grid-cell at  $x$ ,  $t_0$  is the time of release, and  $T$  is the integration period (the post-release collection duration).

Following the net analogy, a magnetic-collector acts like a small stationary net that vanes into the flow with an aperture dimension of  $13.3 \times 6.5$  cm, and a model grid-cell as a similar net with a surface-layer grid-cell aperture dimension of  $2 \times 200$  m. To compare the MAP collector results ( $N_{MAP}$ ) with the model exposition results,  $E_{ij}$  was converted to number to account for the differences in the two measurements (number vs. exposition and collector aperture vs. grid-cell aperture). Accordingly, virtual particle number ( $N_{VP}$ ) from exposition in each grid-cell,  $E_{ij}$ , associated with each collector location was calculated as

$$N_{VP} = E_{ij} \cdot \frac{A_{coll} \cdot N_{MAPR}}{A_{cell} \cdot N_{VPR}}, \quad (3)$$

where  $A_{coll}$  is the magnetic-collector aperture area,  $A_{cell}$  is the grid-cell aperture area,  $N_{MAPR}$  is the number of MAPs released at the point source in Murray Harbour, and  $N_{VPR}$  is the number of VPs released at the same location in the model. Each collector-specific  $N_{VP}$  estimate was based on the average  $N_{VP}$  of that collector-specific grid-cell  $N_{VP}$  and the eight surrounding grid-cell  $N_{VP}$  values. With the proportionality constants in Equation (3), the MAP estimates from the magnetic-collector system allow a direct comparison with the VP estimates from the model as they are essentially measuring the same thing – the time integral of particles passing through a location over time.

As none of the  $N_{MAP}$  and  $N_{VP}$  observations were consistent with a normal distribution, they were logarithmically transformed to obtain distributions more consistent with normality for regression purposes. All uncertainties are presented as 95% confidence intervals.

## 2.7. Estimating dispersal kernels

While Equation (2) expresses the MAP or VP captures at each spatial location, the observations can be used to obtain a probability density function that can be considered an estimate of the dispersal kernel. The resulting estimates are equivalent to sampling the two-dimensional dispersal kernel at a finite number of locations over a given sampling period  $T$  and its associated environmental conditions. There may be variability associated with, for example, the neap-spring tidal cycle and (or) season, and replicate releases or a long-term steady release (or multiple model simulations) would be required to obtain an ensemble and (or) time averaged dispersal kernel.

Although dispersal is typically two-dimensional, heterogeneous, and anisotropic (Gawarkiewicz et al., 2007), our preliminary analyses indicated that both  $N_{MAP}$  and  $N_{VP}$  were primarily a function of in-water distance  $L$  between the source and the collector (or model grid cell) locations, allowing estimation of a greatly simplified single-variable dispersal kernel (e.g., Gerrodette, 1981; Largier, 2003). The estimates of the observed number ( $N$ ) of MAPs or VPs are presented in a semilog manner ( $\log_e N$  as a function of  $L$ ) and consistent with the linear relation  $\log_e N = b - aL$ . The linear relation is equivalent to an exponential function,  $n(L) = e^b \cdot e^{-aL}$ , where  $n$  represents the observed number of MAPs or VPs at distance  $L$ , with an  $e$ -folding scale of  $a^{-1}$ . In this case the  $e$ -folding scale is simply the length scale where  $n(L)$  decreases by a factor of  $e$ .

We define the dispersal kernel  $p(r, \theta; t)$  as the probability density function describing the spatial distribution of MAPs or VPs originating from the source location (Nathan et al., 2008). For the sake of definitiveness,  $p(r, \theta; t)$  is the probability density function (units  $\text{m}^{-2}$ ) of a particle that is released at  $r = 0, t = 0$  at any position ( $r, \theta$ ) and later time  $t$ , where  $r$  and  $\theta$  are the radial and azimuthal coordinates, respectively, in the two-dimensional horizontal plane. We wish to estimate the dispersal kernel  $p$  from the observation of MAP or VP integrated capture numbers that are approximated as  $n(L) = e^b \cdot e^{-aL}$ . If we consider  $p$  to be a radially-symmetric function, and ignore the subtlety that the domain includes land, then we can take the in-water distance  $L$  as equivalent to radius. We denote  $P(r \geq L; T)$  as the probability that a particle is located at a distance  $L$  or greater from the release point at time  $T$ , so that

$$P(r \geq L; T) = \int_L^\infty r \, dr \int_0^{2\pi} d\theta \, p(r, \theta; T), \quad (4)$$

where  $P$  on the left is the probability that we can estimate using the data and  $p$  on the right is the probability density function (i.e., the dispersal kernel) that we want to determine. We assume a radially symmetric distribution and that we can estimate the left hand side of (4) functionally by

$$P(L) \equiv P(r \geq L; T) \approx \frac{n(L)}{N_{eff}}, \quad (5)$$

where  $n(L)$  is the regression formula for the fit to  $N_{MAP}$  or  $N_{VP}$  that is  $n(L) = e^b \cdot e^{-aL}$  and  $N_{eff}$  is the “effective” number of MAPs or VPs in the dispersal domain and, particularly for MAPs, is essentially unknown (addressed in Discussion); however, we can rearrange Equation (5) to

$$P(L) = \left( \frac{e^b}{N_{eff}} \right) e^{-aL}, \quad (6)$$

where the rational coefficient is a constant. We require that  $P(L = 0) = 1$  which is the same as  $P(r \geq 0; T) = 1$ ; i.e., the probability of a particle being somewhere is equal to 1, and thus

$$\left(\frac{e^b}{N_{\text{eff}}}\right) = 1. \quad (7)$$

We use Equation (7) as opposed to the regression coefficient  $b$  and the actual number of MAPs ( $N_{\text{MAPR}}$ ) or VPs ( $N_{\text{VPR}}$ ) released because  $N_{\text{MAPR}}$  is not necessarily the number of MAPs available for capture within the dispersal domain. Thus, we have

$$P(L) \equiv P(r \geq L; T) \approx e^{-aL}. \quad (8)$$

Substituting Equation (8) into Equation (4) yields

$$e^{-aL} = \int_L^\infty r \, dr \int_0^{2\pi} d\theta \, p(r, \theta; T), \quad (9)$$

and as we are assuming  $p$  is radially symmetric, then  $p(r, \theta; T) = p(r; T)$ , and Equation (9) becomes

$$e^{-aL} = 2\pi \int_L^\infty r \, p(r; T) \, dr. \quad (10)$$

Taking the derivative of both sides of Equation (10) with respect to  $L$  gives

$$\frac{d}{dL}(e^{-aL}) = 2\pi \frac{d}{dL} \left( \int_L^\infty r p(r; T) \, dr \right), \quad (11)$$

and

$$-ae^{-aL} = 2\pi(-Lp(L; T)). \quad (12)$$

Solving Equation (12) for  $p$  and multiplying both sides by  $2\pi L$  gives an observational estimate of the dispersal kernel:

$$2\pi L p(L; T) = ae^{-aL}. \quad (13)$$

Fitting to an exponential function and normalising in this manner has three advantages: first, the simple form with a single parameter ( $a$ ) is conceptually and analytically useful while retaining accuracy, second, the paucity of observations in the large-distance “tail” of the distribution does not significantly affect the estimation of the dispersal kernel, and third, the analytic function allows estimation of expected results for locations that were not experimentally sampled. Note that the method above can be applied to any function of in-water distance, not just an exponential.

In the results below we plot  $2\pi L \cdot p(L)$  rather than  $p(L)$  because the probability of transport from the source ( $L = 0$ ) to all distances within a specific distance  $D$  is given by  $\int_0^D 2\pi L p(L) \, dL$ , where the quantity  $2\pi L p(L)$  is also known as the “dispersal distance kernel” – the probability density function of distance travelled from the source, regardless of direction (Nathan et al., 2012). The dispersal kernel has an implicit dependence on time  $T$ ; i.e., it represents an estimate arising from the environmental conditions present during the study period, and will depend on the timing and duration of the experiment.

### 3. Results

#### 3.1. MAP dispersion

MAPs were captured by each of the 40 magnetic-collectors that were recovered 5–7 days post-release; i.e., there were no zero returns, though 6 collectors were not recovered (Fig. 1). The spatial distribution of the missing collectors did not appear systematic and

we assumed that the missing data did not compromise our analyses and interpretation thereof. The majority of MAPs among collectors were concentrated near the release location within Murray Harbour. Beyond the Harbour, the particle concentrations among collectors were elevated along the coast and particularly to the south and west along the Murray Head peninsula (Fig. 1). In general, though not necessarily systematically, fewer MAPs were collected toward the northeast with increasing distance from the release location. In the following comparisons of MAPs and VPs, the reader is reminded that the modelled estimates of VPs can potentially span a much larger domain that extends beyond that defined by the collector array.

#### 3.2. VP dispersion

Modelled VP positions at discrete same-phase times over several tidal cycles, up to ~2.5 days post-release, using various  $K_p$  values (Fig. 2), reflected several aspects of the observed MAP concentration distribution illustrated in Fig. 1, particularly along the Murray Head peninsula. We selected the  $K_p$  values shown to first illustrate streakiness from just tidal influences ( $0 \text{ m}^2 \text{ s}^{-1}$ ), a value that is typically used among modellers ( $2 \text{ m}^2 \text{ s}^{-1}$ ), as well as a value large enough such that VPs encompass the entire collector array ( $80 \text{ m}^2 \text{ s}^{-1}$ ). With no small-scale diffusion ( $K_p = 0 \text{ m}^2 \text{ s}^{-1}$ ), the “streaky” nature of the VP field was apparent as it evolved with the tide, transporting the particles south and west along the peninsula ( $T_0$ ) and then folding and reversing north-eastward but further offshore (+2 tidal cycles) and then essentially repeating the tidal evolution (+4 tidal cycles), as well as reflecting particle advection with the tidal residual to the northeast. When  $K_p$  was increased to  $2 \text{ m}^2 \text{ s}^{-1}$ , over the same tidal evolution, the particles became more dispersed to the south and northeast of Murray Head peninsula. Where previously the streaks began to fold and reverse, the increased  $K_p$  produced a more dispersed field with relatively large concentrations aligned with the residual current. Using a minimum  $K_p$  of  $80 \text{ m}^2 \text{ s}^{-1}$ , the resultant dispersive effect was more apparent over the same tidal evolution, though now with particles being dispersed further from the localised concentration.

The VP exposition number estimates (Fig. 3), based on a constant  $K_p$  of  $25 \text{ m}^2 \text{ s}^{-1}$  reflected various aspects of the observed MAP capture number estimates among collectors (Fig. 1). The rationale for choosing a  $K_p$  value of  $25 \text{ m}^2 \text{ s}^{-1}$  is detailed below. A visual comparison of Figs. 1–3 indicates that the model effectively reflected the general features of the observed MAP field. Within the confines of the collector array, the model tended to show low exposition numbers of VPs in areas where the magnetic-collectors captured low numbers of MAPs (typically offshore), as well as high exposition numbers of VPs in areas where the collectors collected high numbers of MAPs (in Murray Harbour and along the Murray Head peninsula). VP exposition number estimates, based on the other constant and minimum  $K_p$  values, illustrated patterns similar to those addressed above, except that the VP dispersion fields did not encompass the entirety of the MAP dispersion field at constant  $K_p$  values of 2 and  $5 \text{ m}^2 \text{ s}^{-1}$  (Fig. S6, S7). At minimum  $K_p$  values of 50 and  $80 \text{ m}^2 \text{ s}^{-1}$ , the VP fields filled the entire model domain, at least to the north and east (Fig. S8, S9).

#### 3.3. MAP and VP comparison

The relation between  $N_{\text{VP}}$  and  $N_{\text{MAP}}$ , based on a constant  $K_p$  of  $25 \text{ m}^2 \text{ s}^{-1}$  (Fig. 4), indicated a significant ( $p < 0.001$ ) and generally linear ( $r^2 = 0.49$ ) relation, though the confidence interval around the expected number of particles estimated by the model ( $N_{\text{VP}}$ ) in relation to the observed ( $N_{\text{MAP}}$ ) was large. Notably, the slope ( $1.00 \pm 0.33$ ) indicates that the relative dilution between MAPs and VPs tends to be proportional, while the intercept ( $2.08 \pm 0.59$ )

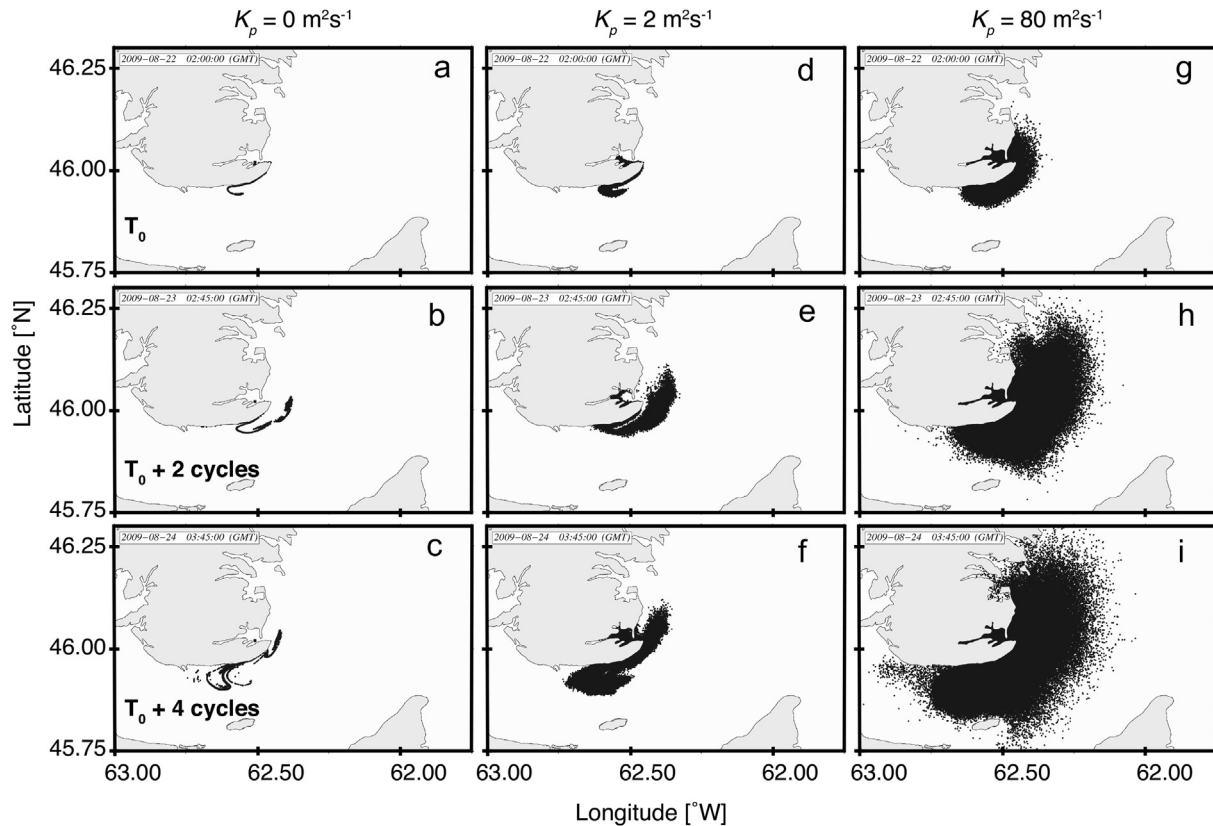


**Fig. 2.** Coastline charts of eastern Northumberland Strait illustrating examples of the near common-phase M2 tidal cycle evolution (ordinate charts) of modelled VP dispersion from the particle release point at Murray Harbour as augmented by the random walk small-scale diffusivities ( $K_p$ , abscissa charts) of 0 (a–c), 2 (d–f), and minimum of  $80 \text{ m}^2 \text{ s}^{-1}$  (g–i). Discrete times on the abscissa charts evolve from  $T_0 = 13.5 \text{ h}$  post-release to two ( $T_0 + 24.8 \text{ h}$ ) and four ( $T_0 + 49.8 \text{ h}$ ) subsequent tidal cycles.

indicates that the model predictions exceeded the MAP captures by two orders of magnitude. In addition,  $N_{VP}$  tended to over-estimate  $N_{MAP}$  as the collector locations progressed from the near field inside Murray Harbour, along the coast and nearshore open water, and progressively under-estimated into the far field offshore open water. This pattern was apparent among all relations between  $N_{VP}$  and  $N_{MAP}$  based on the other  $K_p$  values (Fig. S10 – S13), despite the fact that the slopes of the relations were sensitive to the  $K_p$  values used in the model simulations (Fig. 5, Table S1). At small  $K_p$  values, the slopes were  $>1$  ( $1.66 \pm 0.62$  at  $K_p = 2 \text{ m}^2 \text{ s}^{-1}$  and  $1.44 \pm 0.53$  at  $K_p = 5 \text{ m}^2 \text{ s}^{-1}$ ), and at higher  $K_p$  values, the slopes were  $<1$  ( $0.81 \pm 0.25$  at  $K_p = 50 \text{ m}^2 \text{ s}^{-1}$  and  $0.69 \pm 0.20$  at  $K_p = 80 \text{ m}^2 \text{ s}^{-1}$ ). Based on the 95% confidence intervals around the slope estimates at each of the various  $K_p$  values used, it appears that on average, the appropriate  $K_p$  for modelling this system over the study period lies somewhere around a constant  $25 \text{ m}^2 \text{ s}^{-1}$  that is bracketed by a constant  $5 \text{ m}^2 \text{ s}^{-1}$  and a minimum  $50 \text{ m}^2 \text{ s}^{-1} K_p$ .

#### 3.4. Estimating dispersal kernels

The number of MAPs captured by the collectors decreased exponentially with in-water distance,  $L$ , from the release point (Fig. 6a). The resultant dispersal kernel for the purely passive particles provided an estimated  $e$ -folding scale of 7.15 km with lower and upper 95% confidence limits of 5.19 and 11.44 km, respectively (Fig. 6b).

The uncertainties associated with the decrease in  $N_{MAP}$  at small  $L$  are large and may be related to a relatively rapid and constant proportional decay near the release location within Murray Harbour, followed by a slower and proportionally constant decay

thereafter (Fig. 6a). The 95% confidence intervals around  $2\pi L p_{MAP}(L)$  (not shown) were smaller than those around  $N_{MAP}$  since  $p_{MAP}$  is obtained from a derivative of  $N_{MAP}$  and is affected only by uncertainty in the slope  $a$ , whereas both the slope and intercept, and their respective uncertainties, affect  $N_{MAP}$ . Since the uncertainties associated with the intercept ( $L = 0$ ) were large ( $\pm 0.70$ ; approximately an order of magnitude),  $N_{MAP}(L)$  was not well estimated within the Harbour. Evidence for this is demonstrated by assessing the decrease in  $N_{MAP}$  as a function of  $L$  for the collectors located only within the Harbour, wherein the slope was estimated at  $-1.21 \pm 1.41$  (Fig. S14, S15), relative to  $-0.14 \pm 0.05$  (Fig. 6a) with all collectors included.

The number of VPs estimated among the model simulations also decreased exponentially with  $L$  for each of the  $K_p$  values used (Fig. 7a, S16a–S19a, Table S2), and thus were in general agreement with the decrease in MAPs (Fig. 6a). As  $K_p$  increased, the  $e$ -folding scales for each of the VP dispersal kernel estimates also increased (Fig. 8), with the model again exhibiting a sensitivity to  $K_p$ , as in Fig. 5. When taking the 95% confidence intervals into account, we can conclude that an appropriate  $K_p$  for modelling this system, on average, over the study period, lies somewhere between the minimum  $K_p$  values of 50 and  $80 \text{ m}^2 \text{ s}^{-1}$ , which is greater than is indicated when using the  $N_{MAP}$  and  $N_{VP}$  comparison above (Fig. 5). The  $N_{VP}$  regression on  $L$  from the model simulation using a minimum  $K_p$  of  $80 \text{ m}^2 \text{ s}^{-1}$  (Fig. 7a) provided an  $e$ -folding scale estimate of 5.57 km with upper and lower 95% confidence limits of 6.52 and 4.87 km, respectively, which was comparable to the  $e$ -folding scale estimate of 3.86 km with upper and lower 95% confidence limits of 4.85 and 3.21 km, respectively, when using a constant  $K_p$  of  $25 \text{ m}^2 \text{ s}^{-1}$  (Fig. 7b, S18).

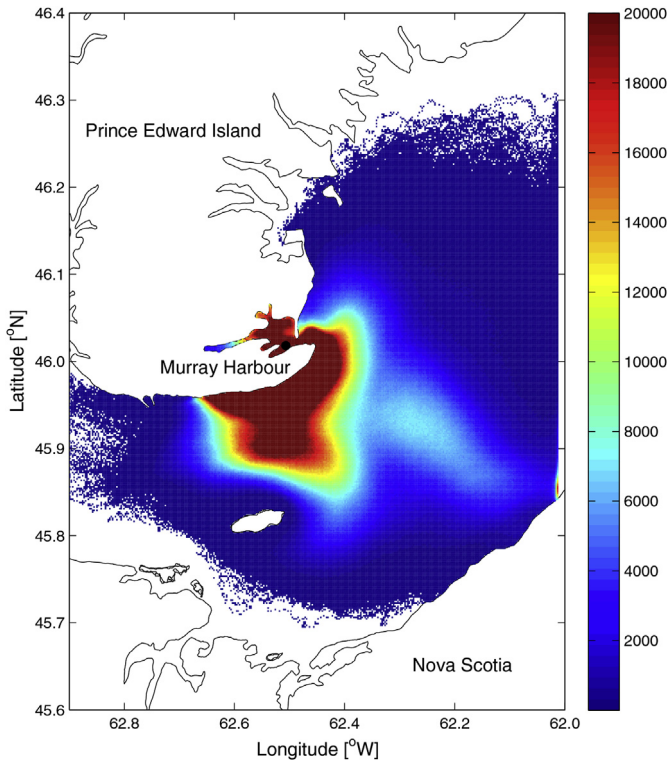


**Fig. 3.** Coastline chart of eastern Northumberland Strait and scale bar illustrating the exposition number,  $E_{ij}$ , of VPs (released at Murray Harbour) within each  $200 \text{ m}^2$  grid cell across the model domain as of 09:00 h on 28 August 2009 and based on a constant  $K_p$  of  $25 \text{ m}^2 \text{ s}^{-1}$ . VPs cannot move beyond the right-hand boundary of the  $200 \text{ m}$  resolution model domain that parallels  $62^\circ\text{W}$  longitude.

In summary, the largest difference in the  $e$ -folding scales lie in the “tails” of the dispersal kernels, which is apparent when comparing that derived from a constant  $K_p$  of  $25 \text{ m}^2 \text{ s}^{-1}$  with that derived using a minimum  $K_p$  of  $80 \text{ m}^2 \text{ s}^{-1}$  (Fig. 7b). Each of the exponential decay relations associated with the  $e$ -folding scales derived using the other  $K_p$  values (Fig. 8) are provided in Figures S16–S19. Again, the reader is reminded that the 95% confidence intervals shown in Fig. 7b are associated with the exponential function,  $N_{VP}$ , and not with the probability density function,  $2\pi L p_{VP}(L)$ .

#### 4. Discussion

##### 4.1. MAP and VP comparison

The spatial distributions of the MAP capture number estimates and the VP exposition number estimates generally agree well (Figs. 1–3) and indicate that the model predictions generally reflect the Lagrangian particle displacements measured using the MAP collectors. The general correspondence between the observed particle collections and the Lagrangian predictions from the model should allow similar model predictions to be made using different environmental conditions, such as variation in the wind field, and (or) release location(s) within the model domain.

In our initial MAP vs. VP number comparisons (e.g., Fig. 4) we focused primarily on the slope of the relation because our aim was to determine the same relative dilution between the observed and modelled estimates (i.e., slope = 1) by varying the small-scale diffusion coefficient,  $K_p$ , in the model. A strong MAP-VP agreement would be reflected in a linear relationship

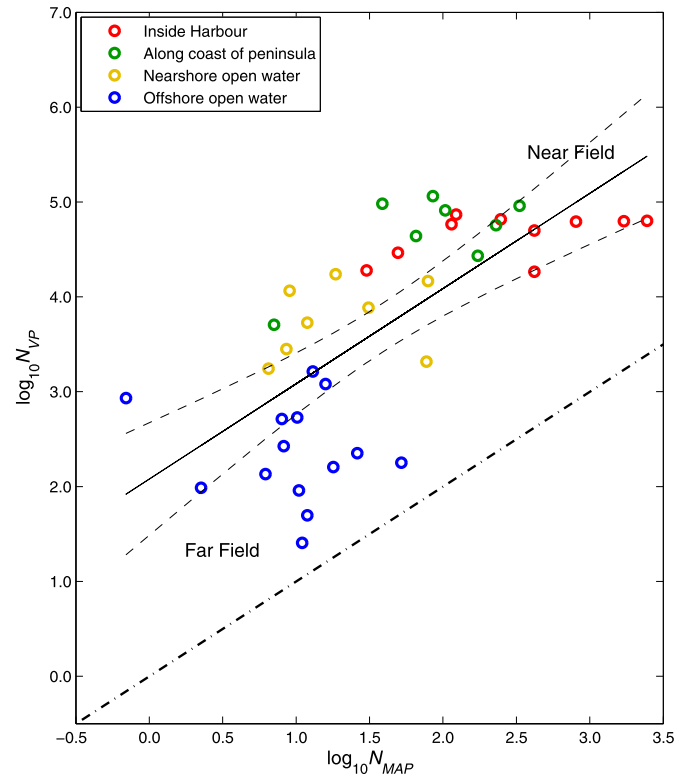


**Fig. 4.** Log–log relation of  $N_{VP}$  as a function of  $N_{MAP}$  where  $N_{VP}$  modelling used a constant  $K_p$  of  $25 \text{ m}^2 \text{ s}^{-1}$ . The regression model [ $\log_{10}N_{VP} = 2.08 + 1.00 \log_{10}N_{MAP}$ ;  $r^2 = 0.49$ ;  $p < 0.001$ ] is illustrated by a solid line with the 95% confidence interval around the model (dashed lines) fitted to the estimates nominally classified as near- to far-field distances from the source inside Murray Harbour (red), along the coast of the peninsula (green), in near-shore open waters (yellow) and offshore open waters (blue). The 1:1 relation is illustrated as a dashed-dotted line.

with a slope of 1.00, and thus examining the relation is the first-order test of the observed particle number distribution ( $N_{MAP}$ ) and the expected particle distribution provided by the model ( $N_{VP}$ ).

In doing so, we demonstrated a sensitivity that the model exhibits to a varying  $K_p$ . We achieved a slope of 1.00 by using a constant  $K_p$  of  $25 \text{ m}^2 \text{ s}^{-1}$  (Fig. 5), though we make no inference that this value of  $K_p$  is the “best” value for modelling this system; this is addressed further below concerning our estimation of the dispersal kernels. A detailed comparison of the MAP and VP dilution rates revealed subtle differences in the slope that appeared to be a function of  $K_p$ . Our results indicate that the “true”  $K_p$  is varying over time and space as illustrated by the seemingly systematic deviations from the regression models as the estimates progress from the near field to the far field. If there were no or small deviations, we could conclude we have identified the “true”  $K_p$  for this system and study period. As this is not the case, a constant value of  $25 \text{ m}^2 \text{ s}^{-1}$  over the entire 7-day study appears to best represent a time and space average of the small-scale diffusivity, though the 95% confidence intervals require a conservative conclusion that  $K_p$  is varying in time and space somewhere between  $5$  and  $50 \text{ m}^2 \text{ s}^{-1}$ ; considerably higher than the typical value of  $K_p$  we first employed in the model. We suggest that using a typical  $2 \text{ m}^2 \text{ s}^{-1}$  value for modelling similar physical environments is inadequate. Nevertheless, by examining model results among  $K_p$  values in comparison with the MAP estimates, we have provided a practical means of calibrating such models and (or) systems, as well as a means of improving the models.

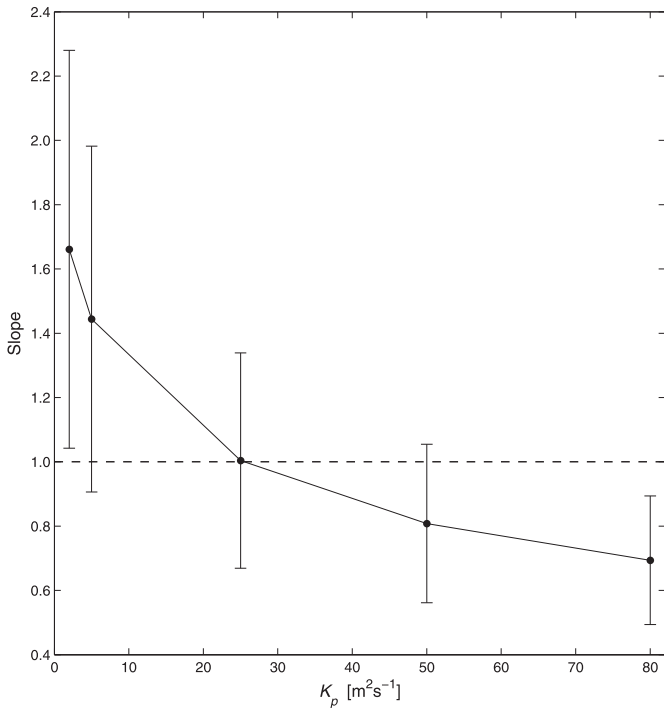


**Fig. 5.** Slopes of the log–log regressions of  $N_{VP}$  on  $N_{MAP}$  (e.g., Fig. 4) as a function of constant (2, 5, and  $25 \text{ m}^2 \text{ s}^{-1}$ ) and minimum (50 and  $80 \text{ m}^2 \text{ s}^{-1}$ )  $K_p$  values used in  $N_{VP}$  modelling, each with their associated 95% confidence intervals. The dashed line illustrates the 1:1 proportional change (i.e., slope = 1).

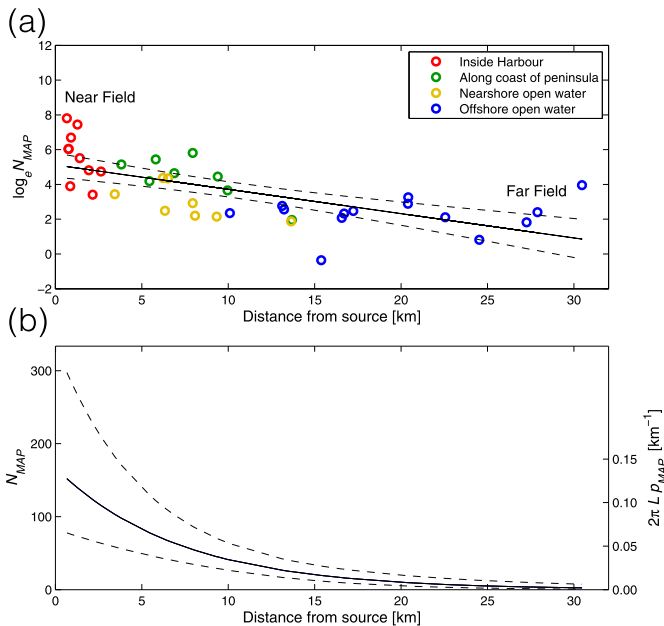


**Fig. 6.** Log-linear (a) and exponential decay (b) of  $N_{MAP}$  as a function of distance,  $L$  (km), from the particle release point (source). The regression model [ $\log_e N_{MAP} = 5.12 - 0.14 L$ ;  $r^2 = 0.43$ ;  $p < 0.001$ ] in (a) is illustrated by a solid line with the upper and lower 95% confidence limits around the model (dashed lines) fitted to the  $N_{MAP}$  estimates nominally classified as near- to far-field distances from the source inside Murray Harbour (red), along the coast of the peninsula (green), in near-shore open waters (yellow) and offshore open waters (blue). The exponential decay [ $N_{MAP} = 1.67 \times 10^2 e^{-0.14 L}$ ] in (b) is illustrated by a solid line with the upper and lower 95% confidence limits (dashed lines). The exponential decay (solid line) can be interpreted as  $2\pi L p_{MAP}$  (right ordinate) with an  $e$ -folding scale of 7.15 km that has upper and lower 95% confidence limits of 11.44 and 5.19 km (see Fig. 8).

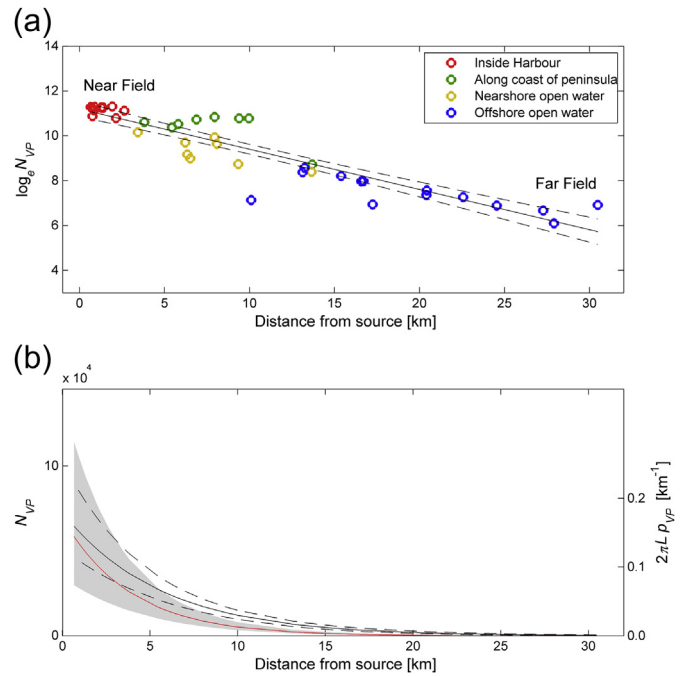


**Fig. 7.** Log-linear (a) and exponential decay (b)  $N_{VP}$  as a function of distance,  $L$  (km), from the particle release point (source) based on a minimum  $K_p$  of  $80 \text{ m}^2 \text{ s}^{-1}$ . The regression model [ $\log_e N_{VP} = 11.19 - 0.18 L$ ;  $r^2 = 0.84$ ;  $p < 0.001$ ] in (a) is illustrated by a solid line with the upper and lower 95% confidence limits around the model (dashed lines) fitted to the  $N_{VP}$  estimates nominally classified as near- to far-field distances from the source inside Murray Harbour (red), along the coast of the peninsula (green), in near-shore open waters (yellow) and offshore open waters (blue). The exponential decay [ $N_{VP} = 7.27 \times 10^4 e^{-0.18 L}$ ] in (b) is illustrated by a solid black line with the upper and lower 95% confidence limits (dashed lines). The exponential decay (solid black line) can be interpreted as  $2\pi L p_{VP}$  (right ordinate) with an  $e$ -folding scale of 5.57 km that has upper and lower 95% confidence limits of 6.52 and 4.87 km (see Fig. 8). The exponential decay [ $N_{VP} = 9.64 \times 10^4 e^{-0.26 L}$ ] based on a constant  $K_p$  of  $25 \text{ m}^2 \text{ s}^{-1}$  is illustrated by the solid red line with the upper and lower 95% confidence limits (shaded). When interpreted as  $2\pi L p_{VP}$ , the  $e$ -folding scale is 3.86 km with upper and lower 95% confidence limits of 4.85 and 3.21 km.

While a slope of 1.00 is achieved for the model simulation comparison using a constant  $K_p$  of  $25 \text{ m}^2 \text{ s}^{-1}$  (Fig. 4), the model over-estimates the MAP numbers by approximately two orders of magnitude, and does so at all values of  $K_p$  used, no matter the slope (Table S1). These elevations can be explained by a number of factors that may be dependent on how the MAPs and the magnetic-collectors behave in the field and (or) on how the model performs in practice.

It is possible that there are MAP losses from the surface layer over time due to sinking and (or) beaching; processes that are not included in the model. It is also possible that the MAPs are so neutrally buoyant that they are vertically mixed throughout the water column, at least to depths greater than 2 m, by tidally- or wind-induced turbulence, and are thus not uniformly available for capture by the magnetic-collectors located near the surface; i.e., the surface layer becomes increasingly diluted by losses to deeper layers, a process that is also not included in the model. Either or both possibilities could explain why the decay in  $N_{MAP}$  estimates in the Harbour (near field) is particularly rapid relative to the far field in relation to  $N_{VP}$  estimates (Fig. 4).

Unresolved issues in the model, some alluded to above, may also help explain the elevations. Although the model resolution (200 m) is respectable for an ocean model, it does not appropriately resolve Murray Harbour due to the size of the Harbour domain and the presence of numerous small islands relative to the grid-cell size and

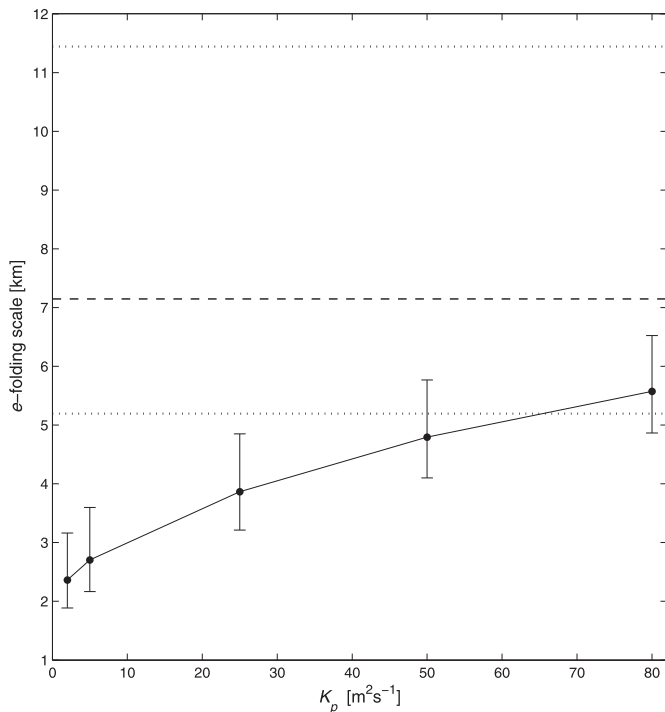


**Fig. 8.** Change in  $e$ -folding scales of the  $N_{VP}$  exponential decay relations (Figs. 5 and 6) as a function of constant (2, 5, and  $25 \text{ m}^2 \text{ s}^{-1}$ ) and minimum (50 and  $80 \text{ m}^2 \text{ s}^{-1}$ )  $K_p$  values with their associated upper and lower 95% confidence limits. The estimated MAP  $e$ -folding scale of the observed dispersal kernel (dashed line) is shown for comparison with the upper and lower 95% confidence limits (dotted lines).

the number of open-water grid-cells. Such a limitation in resolution likely explains why the  $N_{VP}$  estimates in the Harbour (near field) are near constant relative to the far field where the decay is more rapid than that observed by the  $N_{MAP}$  estimates (Fig. 4). In addition, the model does not capture some events well, such as Hurricane Bill, because the wind-field forcing is not highly resolved due to the nature of the wind-field data used for forcing. Finally, as demonstrated above, the sensitivity of the small-scale diffusion applied to the VPs in the model may contribute to the slope elevations. The sensitivity can be rationalised, but not fully explained, by considering mechanisms such as shear dispersion by tidal currents that would be experienced by the MAPs but are not simulated by the model. This sensitivity is addressed below.

#### 4.2. Streakiness, shear dispersion, and model sensitivity to $K_p$

A physical mechanism that explains the dependence of the model predictions on  $K_p$  is illustrated in Fig. 2, which shows the cumulative effect of Lagrangian tidal advection, the dominant stirring mechanism in the region and thus the model. It is clear that dispersion is stronger along the shore to the south and west of Murray Harbour and weaker to the north and the east. It is apparent that the VPs disperse in a complex pattern with numerous streaks that effectively double in number with each tidal cycle, partially due to the continuous release of the VPs over 6 h. Increasing  $K_p$  from  $0 \text{ m}^2 \text{ s}^{-1}$  to  $2 \text{ m}^2 \text{ s}^{-1}$  and to a minimum of  $80 \text{ m}^2 \text{ s}^{-1}$  causes diffusion to fill the gaps between the streaks while retaining a similar overall shape and location of the VP distribution. In theory, an advection-diffusion process could be best-fitted (or approximated) using a diffusion-only model, but this is not what has been simulated here, as the distributional shape of the diffusing VPs ( $K_p = 2 \text{ m}^2 \text{ s}^{-1}$  and  $K_p = 8 \text{ m}^2 \text{ s}^{-1}$ ) retain traits of the advection-only experiment ( $K_p = 0 \text{ m}^2 \text{ s}^{-1}$ ). A diffusion-only model would

demonstrate that an exceedingly high  $K_p$  value would be necessary to achieve any meaningful far field relation with the observed  $N_{MAP}$  estimates; i.e., only when the appropriate advective and diffusive processes are employed do the empirical and modelled results begin to conform (Largier, 2003).

The streakiness observed in Fig. 2 is similar to what we have visually observed in preliminary field trials using the MAPs. It is also similar to that argued by Garrett (1983) and observed by Ledwell et al. (1998) for isopycnal stirring in the deep-ocean thermocline, caused in our case by lateral stirring in the tidal currents (Ridderinkhof and Zimmerman, 1992). Tracer streaks are repeatedly multiplied by the stretching and folding action that is an essential part of “chaotic stirring” (Aref, 1984; Zimmerman, 1986; Ottino, 1990; Thompson et al., 1997). The processes involved in forming the streaks and the diffusion among them are likely responsible for the sensitivity in the model predictions to  $K_p$ ; thus, the comparisons between  $N_{MAP}$  and  $N_{VP}$  serve to help constrain the appropriate small-scale diffusivity in the model.

The details of mixing behaviour depend on the transverse streak spacing ( $L \sim 1\text{--}5 \text{ km}$ ), the tidal period ( $T = 12.42 \text{ h}$ ), and the small-scale diffusivity. We thus expect that model sensitivity to the small-scale diffusivity will occur as long as particles diffuse a distance  $< L$  in  $T$ , corresponding to a diffusivity of  $L^2/T \approx 20\text{--}500 \text{ m}^2 \text{ s}^{-1}$  and not dissimilar to the estimates employed in our model simulations (Fig. 5). Diffusivities smaller than the above allow streakiness to persist and diffusivities larger than the above will “smooth” over the streaks and reduce the sensitivity.

How can the agreement between the modelled VP and the observed MAP number estimates be affected by a model diffusivity enhanced beyond the nominal value of  $2 \text{ m}^2 \text{ s}^{-1}$ ? One possibility that is known to occur physically, but is not explicitly included in the numerical model, is shear dispersion that arises from a combination of vertical mixing and vertically sheared currents. The MAPs have a weak positive buoyancy, with rise rate,  $w_p$ , of  $1\text{--}4 \text{ mm s}^{-1}$ . Zimmerman (1986) gives the velocity of turbulent eddies,  $w'$ , as approximately  $5 \times 10^{-3} u_t$ , where  $u_t$  is the horizontal tidal current velocity, so that if  $u_t$  is  $0.5 \text{ m s}^{-1}$ , then  $w'$  would be  $\sim 2.5 \text{ mm s}^{-1}$ , comparable to the rise rate of the MAPs. It is therefore possible that the tidal currents in the Strait generate sufficiently strong turbulence to mix the MAPs within the water column, and if so mixed, the MAPs would experience shear dispersion, while in the model, the VPs are constrained to the upper  $z$ -layer ( $0\text{--}2 \text{ m}$ ). Zimmerman (1986) reviews models and observations for the tidal vertical shear contribution to dispersion and shows that the equivalent (effective) corresponding horizontal diffusion coefficient is typically in the range of  $10\text{--}25 \text{ m}^2 \text{ s}^{-1}$ , with a strong spatial dependence related to depth and tidal current variation. We have shown above that this is sufficient to cause lateral diffusion among streaks within a tidal period.

In summary, the slow rise rate of the MAPs could allow them to be vertically mixed in the water column by tidally-generated turbulence and thus they would be dispersed by vertical shear. The VPs are constrained to remain in the modelled surface layer and are unaffected by shear dispersion. While we have demonstrated reasonable agreement between  $N_{VP}$  and  $N_{MAP}$  it was improved by imposing a small-scale diffusivity in the model large enough to simulate constant and spatially uniform shear dispersion.

#### 4.3. Estimating dispersal kernels

We have demonstrated the ability of a new, empirical method to directly estimate the passive component of a particle dispersal kernel in a marine system. As the null model of propagule or particulate contaminant dispersal, the physical connectivity estimates can be applied, in the geographic area in question, to any passive

planktonic organism or particulate resident in the surface mixed layer. In this study region we estimated that the MAP-based dispersal kernel has an  $e$ -folding scale of 7.15 km, which is approximately twice the width of Murray Harbour, and approximately the same size as its length. This scaling argument implies that there is considerable potential for retention in the Harbour that may favour local endemic populations, invasive species, or contaminants that may find their way into the Harbour via shipping or other vectors. For example, if the dispersal kernel in Equation (13) above is represented as  $p(L) = (2\pi L)^{-1}ae^{-aL}$ , when  $a^{-1}$  is  $\sim 0.85$  km, similar to the  $e$ -folding scale of the dispersal kernel within Murray Harbour (i.e., Fig. S14, S15), the probability of passive retention within a distance  $D$  and over time  $T$  is  $\int_0^D 2\pi L p(L) dL = \int_0^D ae^{-aL} dL = 1 - e^{-aD}$ . Assuming that  $D$  is 7 km for the length of the Harbour, the probability of retention is 0.9973. Note that this estimate does not address directed swimming or mortality or subtleties associated with directional dispersal or irregular coastline. Similar arguments imply that exported propagule or particulate concentrations diminish rapidly over relatively short length scales. For another example, at a distance of 28 km from the source (i.e., 4  $e$ -folding scales of 7.15 km in our study for the entire domain), the number of particles would fall to  $1/e^4 = 1.80\%$  of the original number, and at 42 km to 0.20%, thus limiting dispersal and hence connectivity over large distances. We have also shown that  $p_{MAP}(L)$  is not well estimated within the Harbour (Fig. S14, S15) if near field Harbour estimates are used along with the far field estimates in determining the dispersal kernel because the  $e$ -folding scale is much lower at  $\sim 0.85$  km. Thus, concentrations in the Harbour decrease far more rapidly with distance relative to outside the Harbour, thereby further limiting connectivity. These empirical estimates of dispersal can provide context in the dispersal of a localised invasive species. For example, the retention of the invasive vase tunicate (*Ciona intestinalis*) within Prince Edward Island harbours (e.g., Kanary et al., 2011) may impact local bivalve aquaculture industry, and larval dispersal ability has implications to management of both the industry and the invasion. Thus, we conclude that estimating dispersal kernels in coastal environments requires very careful consideration of semi-enclosed and nearshore waters separately from open-ocean waters as the consequences may be considerable.

Although linear regression models (e.g., Figs. 6 and 7) have the advantage of a simplified single-parameter dispersal kernel that represents the observations reasonably, although not perfectly well, any experimental observations of MAP captures can be similarly used to yield the probability of spatial transfer from source (release) to sink (collector) locations, giving direct observations of the physical component of the dispersal kernel. In complex physical geometries, with non-uniform flows and non-uniform and anisotropic dispersion, the dispersal kernel could take virtually any (one- or two-dimensional) form, and could reasonably be expected to depend on sink location; i.e., as a two-dimensional function. In light of this, it is quite remarkable that given the complexity of Murray Harbour and eastern Northumberland Strait, a region of anisotropic and non-uniform dispersion confounded by complex shoreline geometry, that a simple exponential function gives a reasonable representation of the dispersal probability by using a single parameter; the  $e$ -folding scale. It is additionally surprising and gratifying that the dispersal kernel estimated using the numerical model is similarly simple, and that the residual variability (deviations from the linear fit) are similar in the model and in the observations.

The magnetic-collectors sample a single realisation of the probability density function, as illustrated above (Figs. 1 and 3), to within a normalisation factor required to give an integrated

probability of 1. The collector array design in our study demonstrated remarkable efficacy in that the bulk of the distribution appears to have been sampled with sufficient detail to capture the structure, and yet with sufficiently smooth results that over-sampling was not apparent. The smooth results are likely associated with the time-integration estimate that the collectors provide, because any streaks of MAPs that occur at intermediate stages of dispersal are swept through collectors, and thus the collectors yield MAP numbers that are not sensitive to their precise locations. The collectors sampled a single dispersal realisation under specific environmental conditions, and this results in a sampling uncertainty that is difficult to quantify without knowledge of the two-dimensional dispersal kernel. Additionally, having collectors at a finite number of locations in the far field, where probabilities are small and areas are large, makes computation of the appropriate kernel difficult. For these reasons, we chose to present our dispersal kernels in one-dimension. Further,  $p_{MAP}$  and  $p_{VP}$  are primarily a function of in-water distance,  $L$ , so that available observations are more parsimonious for estimating a one-dimensional dispersal kernel than a two-dimensional one. We suggest that the simplified one-dimensional dispersal kernel may not be unique to the chosen release location or environmental conditions, but may be representative of the Northumberland Strait region where similar tidal and residual currents are present. Analyses of other MAP studies in this region will allow us to test this hypothesis.

As in the MAP-VP comparisons above (Fig. 5), the VP  $e$ -folding scales also exhibit sensitivities to the small-scale diffusion value (Fig. 8). To approach the MAP  $e$ -folding scale estimate, the model  $K_p$  had to be raised to at least a minimum value of  $50 \text{ m}^2 \text{ s}^{-1}$ . This reflects our inference above that there may not be one “best” value of  $K_p$  when modelling this system. Further, we determined that nearly the entire exponential decay relation (including the 95% confidence limits) for a constant  $K_p$  of  $25 \text{ m}^2 \text{ s}^{-1}$  envelops that for a minimum  $K_p$  of  $80 \text{ m}^2 \text{ s}^{-1}$  (Fig. 7b). The majority of the difference between the two lies in the “tails” of the dispersal kernels, implying that the far field is important for estimating connectivity when using dispersal kernels. For example, the likelihood of survival and establishment of a larva may fall within one  $e$ -folding scale distance, say  $< 5$  km, using either kernel estimate (e.g., Fig. 7b), but potential establishment lies beyond that scale distance in the far field “tails” where the  $p_{VP}$  estimates diverge. Dispersal rates, particularly those of invasive species, are extremely sensitive to the “tail” of the dispersal kernel, and it is often within this “tail” that modelling dispersal becomes problematic (Skarpaas and Shea, 2007; Nathan et al., 2008). We note that when using any value of  $K_p$  in the model, the MAPs have a greater  $e$ -folding scale than the VP estimates provide (Fig. 8). When sub-grid dispersion is employed, others have found that it not only achieves a more realistic model (e.g., Döös et al., 2011), but that models exhibit a sensitivity to this parameter when using values similar to those in our study (e.g., Xue et al., 2008). This suggests, along with our results, that many hydrodynamic models may be too spatially conservative in their dispersal predictions. Sub-grid-scale parameterisations are not well understood and thus not well modelled, and this is a key area in need of improvement when using numerical models (Werner et al., 2007).

Many numerical hydrodynamic models are frequently used as a central tool in MPA planning, invasive species mitigation efforts, the prediction of ecosystem response to changing environmental conditions, source-sink estimation (connectivity), and the dispersal and impact of contaminants. Accordingly, spatially conservative estimates of dispersion, and thus connectivity, may have serious implications and (or) consequences for extant or planned conservation and management. The life-history characteristics of a species

in question, or the source and (or) volatility of a contaminant, will need to be examined in the context of the physical connectivity when making conservation and management decisions. Using such models as first approximations can be highly informative for initial planning purposes and for urgent mitigation responses; however, we argue that when dispersal is a core feature of an issue, such models should not be used to dictate planning and response until they can be tested for the planning and response purposes, and not only the purpose for which they (the models) were originally designed. We suggest that dispersal and model assessment is examined here in a new, strongly Lagrangian manner, and that the MAPs can achieve a quantitative, empirical estimate of the dispersal kernel that has never before been accomplished.

Wunsch (2010) noted that progress in linking empirical observations and model predictions requires combining the information provided by the observations (e.g., the MAPs) with similar information provided by modelling ocean dynamics (e.g., the VPs). According to Wunsch (2010), the combination represents a rare but interdisciplinary field where the practitioners must have a grasp of the powers and pitfalls of the data, the models, and the dynamical theory. He further notes that circulation modelling emerged from geophysical fluid dynamics and computer science when empirical data were sparse and compared with unrealistic numerical models, leading to a community that is disconnected from understanding the observational system. In this context, we hope that our study has made an advance toward linking the empirical with the theoretical.

#### 4.4. Advantages of the MAP and magnetic-collector system

The MAP and magnetic-collector system overcomes many of the issues associated with conventional tracing technologies while providing a direct quantitative measure of dispersal. MAPs can be designed to a specified density and for different shapes and sizes. They are relatively inexpensive, do not degrade easily, and mixtures from different release-sources can be identified. They can be collected over long periods and at large spatial scales using the simple magnetic-collector technology. This system can address a plethora of problems, including invasive species dispersion, egg and larvae dispersion and connectivity, sediment transport, the dispersal of propagules at deep-sea vents, transport and dispersal in aquaculture settings, and the tracing of contaminants, effluent, and river plumes, as well as sewer, storm-water, floc, produced water, and erosion tracing. For a given area, a single experiment can be useful for testing the Lagrangian predictive capabilities of a hydrodynamic model, and the model can thereafter be used with greater confidence to conduct complementary dispersion studies; however, model comparisons under a single set of conditions are not sufficient to confidently extrapolate results to other conditions.

#### Author contributions

J.M.H., J.C., B.R.R., and C.T.T. contributed to the design of the experimental study. J.M.H. and C.T.T. executed the field study and J.C. was responsible for all model simulations. J.M.H. conducted the majority of the analyses and prepared the manuscript with various contributions from all authors. C.T.T. conceived of the MAP technology that was further developed by J.M.H., B.R.R., and C.T.T.

#### Acknowledgements

We express many thanks to A. Szmant, R. Whitehead, and T. Simendinger for perseverance in helping us develop this technology, R. Irani and M. Hatcher who were instrumental in collector design and particle quality control, M. Hatcher, A. Benaroya, and D.

Dwyer for assistance in the field, M. Morgan and K. Kenny-Foeldessy for help in the lab, and J.M. Hanson, M. Merrimen, and W. Judge for logistical support. Technical development and study execution was supported by the Natural Sciences and Engineering Research Council (NSERC) Ideas to Innovation Programme (#322056-05), the NSERC Canadian Healthy Oceans Network (CHONE; #NETGP 340843-06), Fisheries and Oceans Canada Northumberland Strait Ecosystem Research Initiative (NSERI – J.M. Hanson; #F4764-080004) and in part by the U.S.A. National Science Foundation and by Innovacorp I-3 Technology funds. Finally, we thank the anonymous referees and colleagues F. Broell, C.C. Smith, and K. Thompson who were quick to grasp the utility of our work and approach and offered valuable comments that helped to clarify the manuscript.

#### Appendix A. Supplementary data

Supplementary data related to this article can be found at <http://dx.doi.org/10.1016/j.ecss.2013.06.023>.

#### References

- Aiken, C.M., Navarrete, S.A., Castillo, M.I., Castilla, J.C., 2007. Along-shore larval dispersal kernels in a numerical ocean model of the central Chilean coast. *Marine Ecology Progress Series* 339, 13–24.
- Aref, H., 1984. Stirring by chaotic advection. *The Journal of Fluid Mechanics* 143, 1–21.
- Becker, B.J., Levin, L.A., Fodrie, F.J., McMillan, P.A., 2007. Complex larval connectivity patterns among marine invertebrate populations. *Proceedings of the National Academy of Sciences* 104, 3267–3272.
- Begon, M., Harper, J.L., Townsend, C.R., 2006. *Ecology. from Individuals to Ecosystems*, fourth ed. Blackwell Publishing, Malden, p. 738.
- Chassé, J., Miller, R.J., 2010. Lobster larval transport in the southern Gulf of St. Lawrence. *Fisheries Oceanography* 19, 319–338.
- Clobert, J., Danchin, A.A., Dhondt, J.D., 2001. *Dispersal*. Oxford University Press, New York, p. 452.
- Cowen, R.K., Paris, C.B., Srinivasan, A., 2005. Scaling of connectivity in marine populations. *Science* 311, 522–527.
- Cowen, R.K., Gawarkiewicz, G., Pineda, J., Thorrold, S.R., Werner, F.E., 2007. Population connectivity in marine systems. An overview. *Oceanography* 20 (3), 14–21.
- Csanady, G.T., 1982. *Circulation in the coastal ocean*. D. Reidel Publishing Company, Dordrecht, p. 279.
- Döös, K., Rupolo, V., Brodeau, L., 2011. Dispersion of surface drifters and model-simulated trajectories. *Ocean Modelling* 39, 301–310.
- Fogarty, M.J., Botsford, L.W., 2007. Population connectivity and spatial management of marine fisheries. *Oceanography* 20 (3), 112–123.
- Garrett, C., 1983. On the initial streakiness of a dispersing tracer in two- and three-dimensional turbulence. *Dynamics of Atmospheres and Oceans* 7, 265–277.
- Gawarkiewicz, G., Monismith, S., Largier, J., 2007. Observing larval transport processes affecting population connectivity. Progress and challenges. *Oceanography* 20 (3), 40–53.
- Gerrodette, T., 1981. Dispersal of the solitary coral *Balanophyllia elegans* by demersal planular larvae. *Ecology* 62 (3), 611–619.
- Hjort, J., 1914. Fluctuations in the Great Fisheries of Northern Europe. *Rapports. In: Conseil Permanent International pour l'Exploration de la Mer*, vol. 20, pp. 1–13.
- Jones, G.P., Srinivasan, M., Almany, G.R., 2007. Population connectivity and conservation of marine biodiversity. *Oceanography* 20 (3), 100–111.
- Kanary, L., Locke, A., Watmough, J., Chassé, J., Bourque, D., Nadeau, A., 2011. Predicting larval dispersal of the vase tunicate *Ciona intestinalis* in a Prince Edward Island estuary using a matrix population model. *Aquatic Invasions* 6 (4), 491–506.
- Kinlan, B.P., Gaines, S.D., 2003. Propagule dispersal in marine and terrestrial environments: a community perspective. *Ecology* 84, 2007–2020.
- Kinlan, B.P., Gaines, S.D., Lester, S.E., 2005. Propagule dispersal and the scales of marine community process. *Diversity and Distributions* 11, 139–148.
- Largier, J.L., 2003. Considerations in estimating larval dispersal distances from oceanographic data. *Ecological Applications* 13, S71–S89.
- Lauzier, L.M., 1965. Drift bottle observations in Northumberland Strait, Gulf of St. Lawrence. *Journal Fisheries Research Board of Canada* 22, 353–368.
- Ledwell, J.R., Watson, A.J., Law, C.S., 1998. Mixing of a tracer in the pycnocline. *Journal of Geophysical Research* 103, 499–529.
- Levin, L.A., 2006. Recent progress in understanding larval dispersal: new directions and digressions. *Integrative and Comparative Biology* 46, 282–287.
- Nathan, R., 2006. Long-distance dispersal of plants. *Science* 313, 786–788.
- Nathan, R., Schurr, F.M., Spiegel, O., Steinitz, O., Trakhtenbrot, A., Tsoar, A., 2008. Mechanisms of long-distance seed dispersal. *Trends in Ecology & Evolution* 23, 638–647.

- Nathan, R., Klein, E., Robledo-Anuncio, J.J., Revilla, E., 2012. Dispersal kernels: review. Chapter 15. In: Clobert, J., Baguette, M., Benton, T.G., Bullock, J.M., Ducatez, S. (Eds.), *Dispersal Ecology and Evolution*. Oxford University Press, Oxford, p. 496.
- Ottino, J., 1990. *The Kinematics of Mixing: Stretching, Chaos, and Transport*. Cambridge University Press, Cambridge, p. 364.
- Pineda, J., Hare, J.A., Sponaugle, S., 2007. Larval transport and dispersal in the coastal ocean and consequences for population connectivity. *Oceanography* 20 (3), 22–39.
- Rasmussen, L.L., Cornuelle, B.D., Levin, L.A., Largier, J.L., Di Lorenzo, E., 2009. Effects of small-scale features and local wind forcing on tracer dispersion and estimates of population connectivity in a regional scale circulation model. *Journal of Geophysical Research* 114. <http://dx.doi.org/10.1029/2008JC004777>.
- Ridderinkhof, H., Zimmerman, J., 1992. Chaotic stirring in a tidal system. *Science* 258, 1107–1111.
- Ruddick, B.R., Taggart, C.T., 2006. Apparatus, System and Method for Evaluating Fluid Systems. U.S.A. and Canada Patent Pending, Appl. No.11/458,287, Filed 07/18/2006. Conf. #8539, with benefit of 60/699,845 filed 07/18/2005.
- Ruddick, B.R., Taggart, C.T., 2011. A new approach to tracing particulates from produced water. In: Lee, K., Neff, J. (Eds.), *Produced Water*. Springer Science+Business Media, New York, pp. 249–257.
- Sale, P.F., Cowen, R.K., Danilowicz, B.S., Jones, G.P., Kritzer, J.P., Lindeman, K.C., Planes, S., Polunin, N.V.C., Russ, G.R., Sadovy, Y.J., Steneck, R.S., 2005. Critical science gaps impede use of no-take fishery reserves. *Trends in Ecology and Evolution* 20, 74–80.
- Saucier, F.J., Chassé, J., 2000. Tidal circulation and buoyancy effects in the St. Lawrence Estuary. *Atmosphere-Ocean* 38, 505–556.
- Siegel, D.A., Kinlan, B.P., Gaylord, B., Gaines, S.D., 2003. Lagrangian descriptions of marine larval dispersal. *Marine Ecology Progress Series* 260, 83–96.
- Skarpaas, O., Shea, K., 2007. Dispersal patterns, dispersal mechanisms, and invasion wave speeds for invasive thistles. *The American Naturalist* 170 (3), 421–430.
- Smagorinski, J., 1963. General circulation experiments and primitive equations. I. The basic experiment. *Monthly Weather Review* 91, 99–164.
- Thompson, K.R., Shen, Y., Ruddick, B.R., 1997. Dispersion of passive tracers by the oscillating flow of a homogeneous fluid over an isolated topographic feature. In: *Oceanology International 97 Pacific Rim: Extending the Reach of Ocean Technologies*, Conference Proceedings, vol. 1, pp. 301–312.
- Thorrold, S.R., Jones, G.P., Hellberg, M.E., Burton, R.S., Swearer, S.E., Neigel, J.E., Morgan, S.G., Warner, R.R., 2002. Quantifying larval retention and connectivity in marine populations with artificial and natural markers. *Bulletin of Marine Science* 70, 291–308.
- Werner, F.E., Cowen, R.K., Paris, C.B., 2007. Coupled biological and physical models. Present capabilities and necessary developments for future studies of population connectivity. *Oceanography* 20 (3), 54–69.
- Wunsch, C., 2010. Towards understanding the Paleoocean. *Quaternary Science Reviews* 29, 1960–1967.
- Xue, H., Incze, L., Xu, D., Wolff, N., Pettigrew, N., 2008. Connectivity of lobster populations in the coastal Gulf of Maine. Part I: circulation and larval transport potential. *Ecological Modelling* 210, 193–211.
- Zimmerman, J., 1986. The tidal whirlpool: a review of horizontal dispersion by tidal and residual currents. *Netherlands Journal of Sea Research* 20, 133–154.